JOURNAL OF GEOPHYSICAL RESEARCH, VOL. 105, NO. B11, PAGES 25,655–25,670, NOVEMBER 10, 2000

Crustal deformation near Hengill volcano, Iceland 1993-1998: Coupling between magmatic activity and faulting inferred from elastic modeling of satellite radar interferograms

Kurt L. Feigl,[1] Jérôme Gasperi,[2] Freysteinn Sigmundsson,[3] and Alexis Rigo[1]

Abstract. Tectonic activity in the Hengill volcanic area in southwestern Iceland accelerated in July 1994, when an unusually persistent swarm of moderate-sized earthquakes began. Although the largest events were magnitude 5, the pattern of upward crustal deformation at 2 cm/yr indicates that most of the activity is related to inflation of a magma chamber at depth. To monitor this activity, we analyze synthetic aperture radar (SAR) images acquired by the ERS-1 and ERS-2 satellites between July 1993 and September 1998 using interferometry. Interferograms composed of images acquired during the snow-free summer months remain coherent on Holocene lava flows, even after 4 years. Some of the interferograms show a discontinuity in the fringe pattern, which we interpret as 8 mm of (aseismic) dip slip on a 3-km-long segment of a N5°E striking normal fault, part of which had been mapped previously. This slip must have occurred between July 31 and September 3, 1995 (inclusive), and has been confirmed by observations in the field. The predominant signature in all the interferograms spanning at least 1 year, however, is a concentric fringe pattern centered just south of the Hrómundartindur volcanic center. This we interpret as mostly vertical uplift caused by increasing pressure in an underlying magma source. The volume source that best fits the observed interferograms lies at 7 ± 1 km depth and remains in the same horizontal position to within 2 km. It produces 19 ± 2 mm/yr of uplift. This deformation accumulates as elastic strain energy at a rate 2.8 times the rate of seismic moment release. Accumulated over 5 years, it increases the Coulomb failure stress by > 0.6 bar in an area that includes some 84% of the earthquakes recorded between 1993 and 1998. Under our interpretation, magma is injected at 7 km depth, just below the seismogenic zone formed by colder, brittle rock. There the inflation induces stresses that exceed the Coulomb failure criterion, triggering earthquakes, possibly in a cyclical fashion.

1. Introduction

The Iceland hotspot lifts the Mid-Atlantic Ridge above sea level, exposing it to view and offering a unique opportunity to study the mechanical coupling between magmatic activity and faulting. Here we use interferometric analysis of synthetic aperture radar images (INSAR) acquired by satellite to test the hypothesis that increasing magma pressure below the Hengill volcanic area can trigger earthquakes on nearby faults.

The average spreading rate in south Iceland, 18.6 mm/yr, affects two parallel rift zones, known as the Western and Eastern Volcanic Zones (WVZ and EVZ) (Figure 1a). These zones are connected by a transform zone, called the South Iceland Seismic Zone (SISZ). At the Hengill triple junction, the SISZ and the WVZ meet the Reykjanes Peninsula oblique rift. Where it crosses the populated lowland the SISZ is characterized by mapped fault traces, instrumentally determined epicenters, and historical earthquake damage. It is 70−80 km long (E-W) and 20−30 km wide (N-S). Here earthquakes occur on an array of faults striking N-S, perpendicular to the transform trend in "bookshelf faulting" style [*Einarsson,* 1991; *Sigmundsson et al.,* 1995].

The Hengill triple junction is named after the Hengill volcanic system (He), the current focus of tectonic activity in the area (Figure 1b). It is associated with a high-temperature geothermal zone from which hot water is extracted through drill holes. The Hengill central volcano and its transecting fissure swarm, extending from the coast south of Hengill to north of Lake Thingvallavatn, form the Hengill volcanic system. Another active but less pronounced volcanic system, called Hrómundartindur (Hr), lies to the east of the Hengill system. Here geodetic measurements show uplift and expansion of the area, consistent with a pressure increase beneath the center of this volcanic system [*Sigmundsson et al.,* 1997a]. A third volcanic system, Grensdalur (Gr), lies to the south of Hr, but is not as active as either Hr or He.

[1]UMR 5562, Centre National de Recherche Scientifique, Toulouse France

[2]UMR 5562, Université Paul Sabatier, Toulouse, France

[3]Nordic Volcanological Institute, Reykjavik, Iceland

Paper number 2000JB900209.
0148-0227/00/2000JB900209$09.00

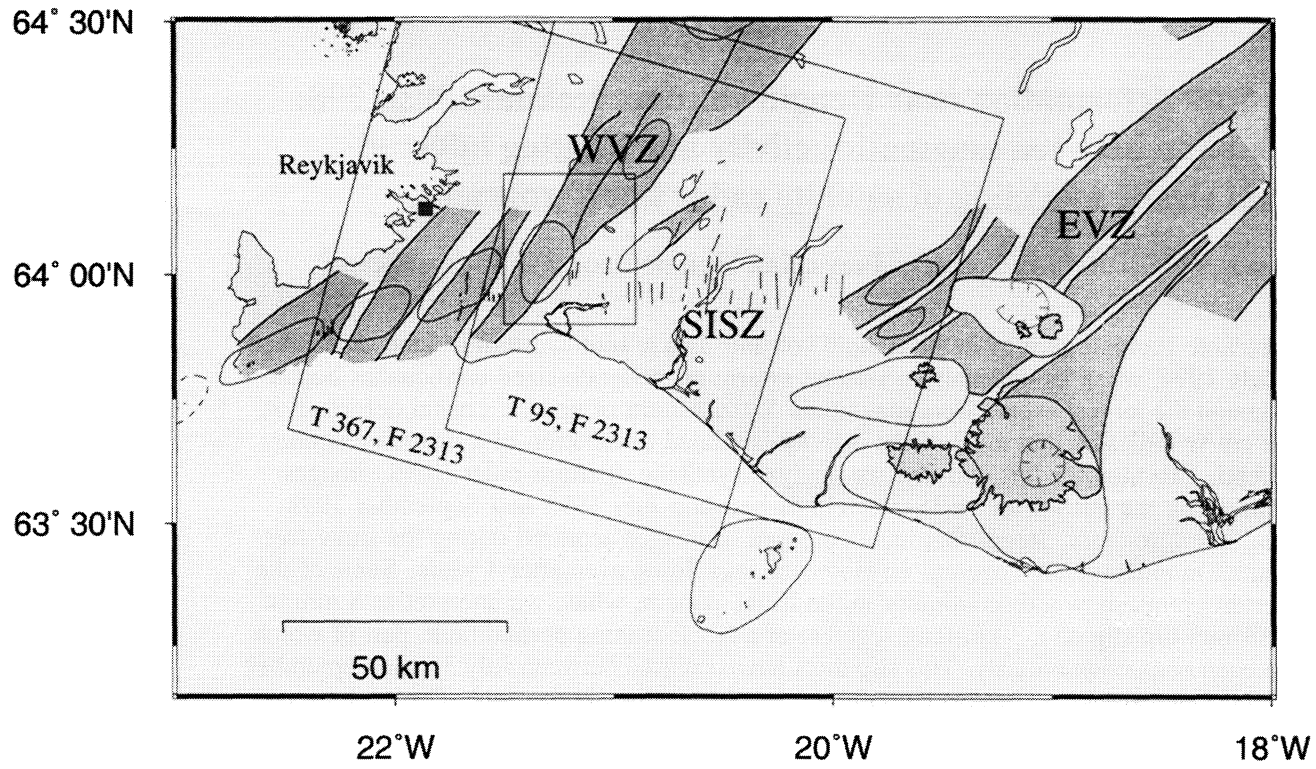

Figure 1a. The South Iceland Seismic Zone (SISZ) between the Eastern and Western Volcanic Zones (EVZ and WVZ), showing mapped, predominantly strike slip, faults (north-south trending solid lines), volcanic systems (dark shaded areas) with their central volcanos (round, solid curves), glaciers (hatched curves), and the mid-Atlantic Ridge (dashed line). The large boxes delimit ERS image frame 2313 of tracks 95 and 367. The small box shows the study area.

The Hengill triple junction exhibits the highest level of continuous seismicity in Iceland [*Einarsson,* 1991]. About half of the earthquake focal mechanisms imply normal and strike-slip faulting in response to the extensional NW-SE tectonic stress. The other half are mostly located in areas of geothermal activity and show evidence of non-double-couple mechanisms with extensional failure due to circulating groundwater [*Einarsson,* 1991]. Seismic tomography reveals a body with high P wave velocity and three pipe-like structures with anomolously low V_p/V_s ratios beneath these three volcanic systems [*Miller et al.,*1998; A. Tryggvason et al., unpublished manuscript, 2000].

In July 1994, an unusually persistent swarm of earthquakes began at the Hengill triple junction. The swarm activity, with most magnitudes < 4, continued through 1999. Most fault plane solutions are strike-slip on subvertical faults [*Rognvaldsson et al.,* 1998a]. The epicenters cluster around the center of the Hrómundartindur volcanic system. Leveling and GPS measurement show a few centimeters of uplift and extension across the area between 1992 and 1995 [*Sigmundsson et al.,* 1997a], continuing through 1998 [*Hreinsdottir,* 1999].

The seismicity rate increased again in two separate sequences during June and November 1998 [*Rognvaldsson et al.,* 1998b]. The sequential rupturing of distinct fault segments in temporally separate clusters may be the result of stress transfer (Thora Arnadottir, written communication, 1999). We are concerned that such earthquakes may load even larger, through-going faults, threatening the population. Such a triggering mechanism may explain the earthquake sequences of 1732, 1784, and 1896 in the South Iceland Seismic Zone [*Einarsson,* 1991] just as observed on the North Anatolian Fault [*Hubert-Ferrari et al.,* 2000].

In this paper, we focus on Hengill using INSAR to measure crustal deformation with dense spatial coverage (100 pixels/km^2) and monthly sampling in the summer months between 1993 and 1998. By describing those observations with an elastic model, we seek to understand the mechanism driving the deformation, especially how the presumably continuous magmatic activity can trigger the episodic faulting.

2. Data and Method

We apply radar interferometry, using synthetic aperture radar (SAR) images acquired by the two European Space Agency (ESA) European Remote Sensing (ERS) satellites. The phase difference between two such images acquired at different times creates an interference (fringe) pattern called an interferogram [*Massonnet and Feigl,* 1998]. The interferograms show the change in range from ground to satellite, that is, the component of the displacement vector which points toward the satellite. Between two fringes of the same

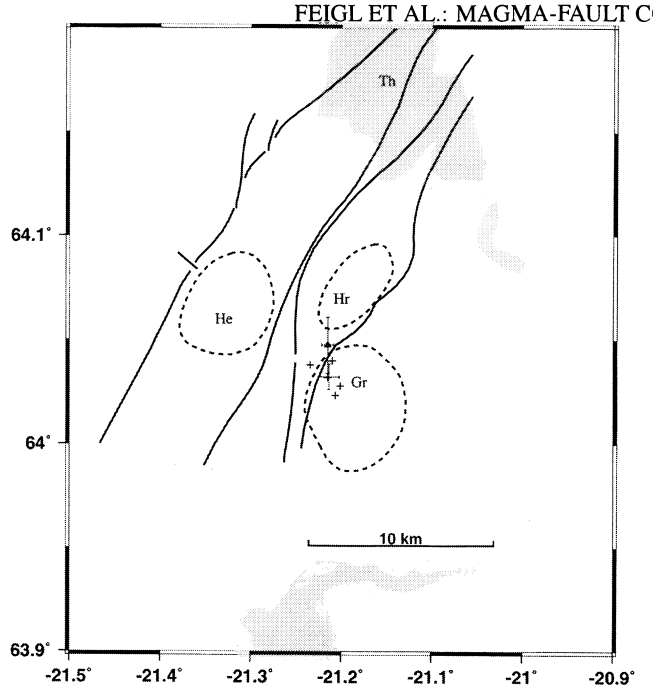

Figure 1b. Study area enlarged in Plate 1. The dashed circles show the three central volcanoes, Hengill (He), Hrómundartindur (Hr), and Grensdalur (Gr) of the Hengill triple junction. Crosses show location of volcanic volume source estimated from various interferograms. Small, crossed error bars indicate best fitting time-averaged location. Triangle indicates location from GPS and leveling [*Sigmundsson et al.,* 1997a]. Shaded area (Th) is Lake Thingvallavatn.

color, there is 28 mm of range change. Such an interferogram records crustal deformation during the time interval between the acquisitions of the two images.

This method has been successfully applied to other volcanos as recently reviewed by *Massonnet and Sigmundsson* [2000]. In Iceland, SAR interferometry has measured significant deformation on the Reykjanes Peninsula [*Vadon and Sigmundsson,* 1997] and in the Northern Rift Zone [*Sigmundsson et al.,* 1997b].

Like these studies, we use the two-pass approach implemented by the DIAPASON software [*Centre National d'Etudes Spatiales,* 1997]. Since the details of this technique have been described elsewhere, we restrict our discussion to interpreting the interferogram in terms of crustal deformation. For this, we consider interferometric correlation of the two radar images, sensitivity to errors in the topographic model, and atmospheric artifacts.

To produce clear fringes in an interferogram, the two radar images must correlate well. If the radar backscattering properties of the ground change between the acquisition dates of the two images, the fringe pattern breaks down into random, incoherent noise. This is called temporal decorrelation. To minimize decorrelation, we selected only images acquired in the summer months (June through September), when the ground was free of snow. Although interferometric correlation tends to decrease with time, the barren ground surface in Iceland remains fairly constant. We find acceptable coherence over intervals as long as 4 years on lava-covered areas. This lets us measure subtle secular signals of the order of one 28-mm fringe per year.

The second issue in interpreting the interferograms involves the interaction between topography and orbital separation. To quantify this effect, we consider the altitude of ambiguity h_a for an interferometric pair. This is the shift necessary to produce one topographic fringe [*Massonnet and Feigl,* 1998]. The larger the altitude of ambiguity in absolute value, the fewer residual topographic fringes in the interferogram. In other words, an error of ϵ meters in the digital elevation model (DEM) used for the topographic correction will create an artifactual phase change of ϵ/h_a fringe in the interferogram. Using 30 images, we calculated 49 interferograms spanning intervals from 1 day to 5 years [*Gasperi,* 1999]. Table 1 lists the 15 best interferograms with $|h_a| > 50$ m. The DEM we use is a DTED-1 furnished by the Icelandic Geodetic Survey, with a grid interval of 3 arc sec in latitude and 6 arc sec in longitude (pixel size is roughly 90 by 90 m), and a nominal vertical precision of $\epsilon \approx 30$ m.

The third issue involves interferometric artifacts due to atmospheric propagation effects. Our approach is to identify any such artifacts by pair-wise logical analysis of the numerous interferograms [*Massonnet and Feigl,* 1995]. Tropospheric perturbations do not appear to contaminate our results, presumably because the edifice has < 400 m of topographic relief. It is quite different from the 3000-m-high conical form which creates the correlation between tropospheric delay and topographic elevation observed at Mount Etna [*Beauducel et al.,* 2000].

3. Results

In spite of our careful image selection, correlation is poor in some parts of the multiyear interferograms. In the relatively flat and wet lowlands of southern Iceland, where agri-

Table 1. Interferograms Included in Deformation Analysis

Interferogram	t_1	t_2	Δt	h_a
10532_17255	July 21, 1993	Aug. 8, 1998	5.00	-52
10532_7235	July 21, 1993	Sept. 7, 1996	3.10	-287
10761_11973	Aug. 8, 1993	Aug. 4, 1997	4.00	10022
10761_1452	Aug. 6, 1993	July 31, 1995	2.00	-54
10761_21626	Aug. 6, 1993	Sept. 3, 1995	2.10	-611
10761_1953	Aug. 6, 1993	Sept. 4, 1995	2.10	211
21125_22127	July 30, 1995	Oct. 8, 1995	0.20	-226
21125_6963	July 30, 1995	Aug. 19, 1996	1.00	529
1452_11973	July 31, 1995	Aug. 4, 1997	2.00	54
1452_6963	July 31, 1995	Aug. 19, 1996	1.00	481
21626_11973	Sept. 3, 1995	Aug. 4, 1997	1.90	576
1953_11973	Sept. 4, 1995	Aug. 4, 1997	1.90	-215
21898_7235	Sept. 22, 1995	Sept. 7, 1996	1.00	126
2454_17985	Oct. 9, 1995	Sept. 28, 1998	2.90	-2770
6963_11973	Aug. 19, 1996	Aug. 4, 1997	1.00	60

Interferograms are specified by master and slave orbit numbers; time span Δt in years, and altitude of ambiguity h_a in meters.

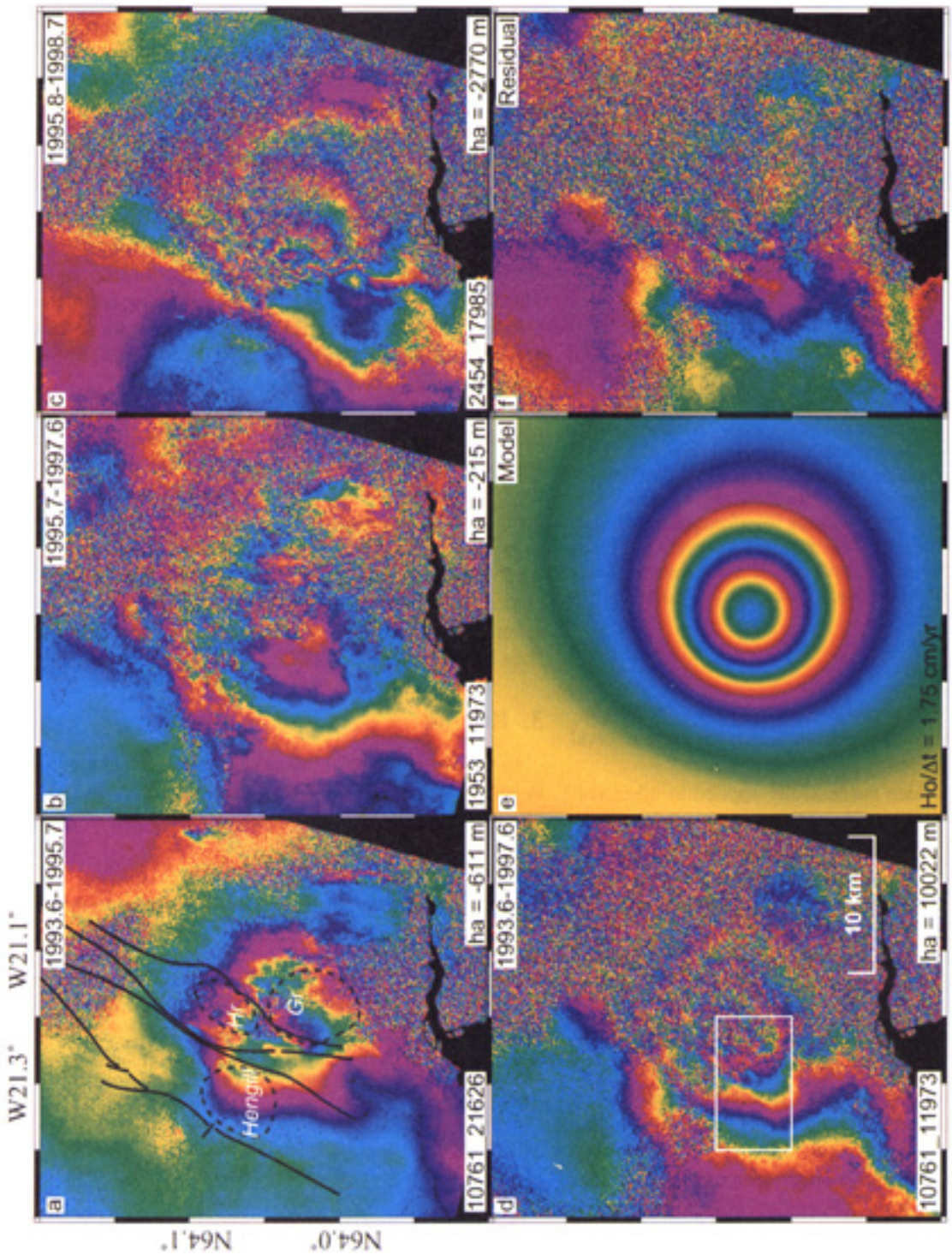

Plate 1. Observed interferograms of the Hengill area for four different time intervals. The time interval appears in the upper right corner of each panel; the orbit numbers appear at lower left; and the altitude of ambiguity h_a appears at lower right. One fringe represents 28 mm of range change. Two concentric fringes are visible in the 4-year interferogram (d) indicating at least 6 cm of uplift between August 1993 and August 1997. The white box in Plate 1d includes the discontinuity enlarged in Plates 2b and 2c. These interferograms have been filtered [*Goldstein and Werner,* 1998]

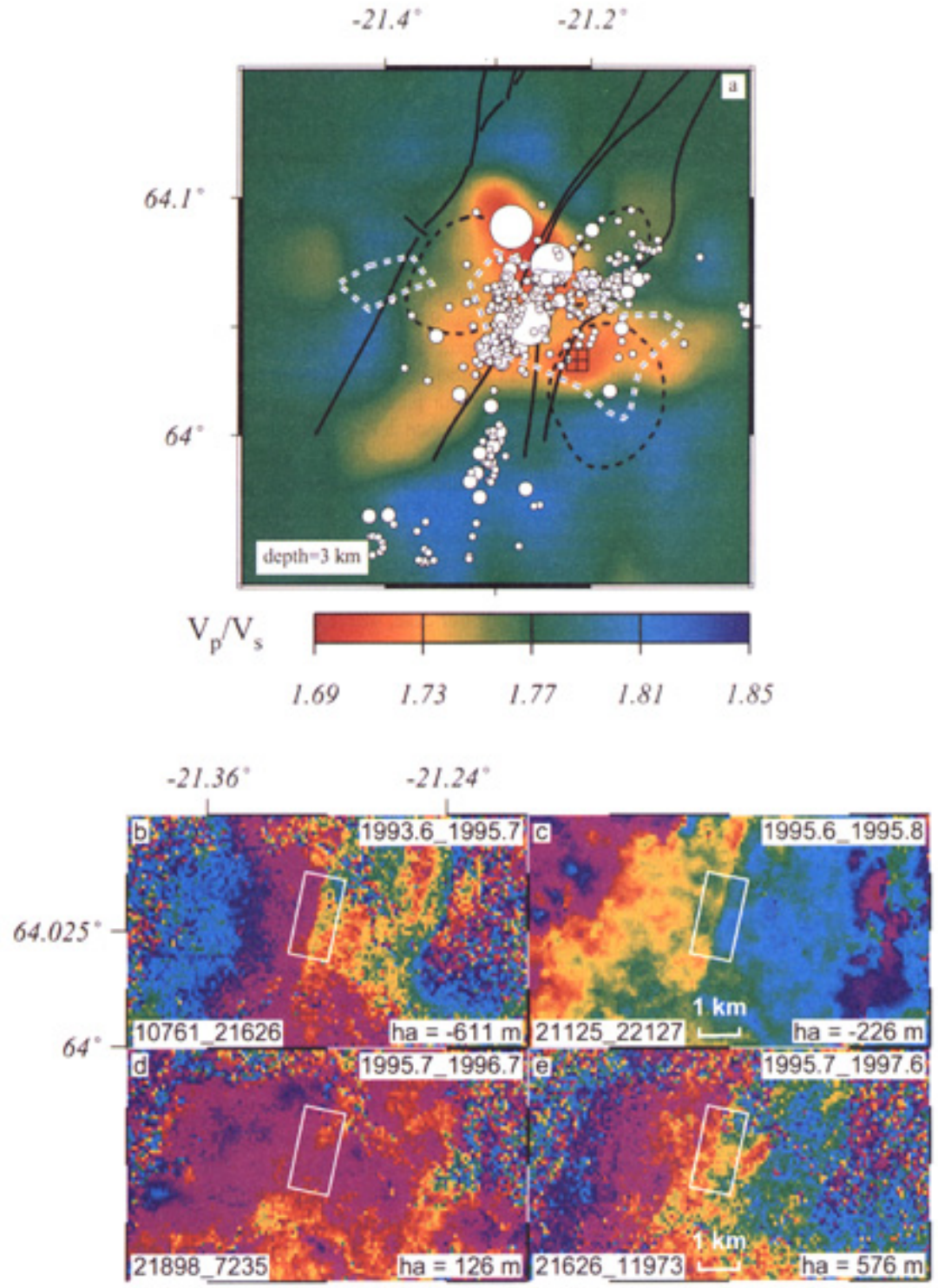

Plate 2. (a) Structural map showing V_P/V_S wave speed ratio at 4 km depth [*Miller et al.,* 1998]; our best fitting volume source (crossed square); contours of P wave speed velocity anomaly $\delta V_P = +1\%$ at 4 km depth (dashed white lines); contours of *Miller et al.,* [1998]; limits of volcanic system (solid black lines); outlines of three central volcanos (dashed black lines). Circles and dots show earthquake hypocenters for events between 1993 and 1998 inclusive [*Rognvalsson et al.,* 1998a, 1998b]. The largest circle is the $M_w = 5.2$ event of June 4, 1998. Events with magnitude smaller than 2.5 plot as dots. (b)-(e) Enlargement of two interferograms that span August 1995 (Plates 2b and 2c) and two which do not (Plates 2d and 2e) A discontinuity is clearly visible in Plates 2b and Plates 2c and is interpreted as a fault rupturing. We cannot discern a discontinuity in Plates 2d and 2e. The white boxes denote the locations of the profiles in Figure 3.

cultural activity abounds, radar correlation breaks down in less than a season. Indeed, even 35-day interferograms show poor coherence in this area, which unfortunately includes most of the faults in the SISZ. On the other hand, coherence remains good, even after 4 or 5 years, in the mountainous areas around Hengill. We attribute this to the barren ground cover of volcanic rocks, especially Holocene basaltic lava flows. Even when mostly covered by decimeter-thick moss heath, the lava flows remain coherent. Since the amount of water contained in the moss varies with time, we attribute the constant reflectivity to the barren rock outcrops protruding from the moss.

The principal signal in the interferograms is a concentric fringe pattern in the Hengill area. All the multiyear interferograms show roughly circular fringes with similar shape and location (Plate 1). Their color changes from red to orange to yellow to green to blue toward the center, indicating that the radar range change $\Delta\rho$ decreases in that direction. We interpret this shortening in the distance between ground and satellite as secular uplift. The number of fringes increases with the time interval Δt. For example, the 4-year interferogram from August 1993 to August 1997 (Plate 1d) shows about twice as many fringes as a 2-year interferogram from September 1995 to August 1997 (Plate 1b).

We can exclude atmospheric artifacts as a cause because many of interferograms combine several independent images, For example, the circular fringes appear in the interferogram spanning August 1993 to September 1995, but also in the interferogram spanning September 1993 to October 1995. These two interferograms have no images in common. Moreover, the values of the altitude of ambiguity h_a exclude the possibility of systematic topographic fringes. For example, the altitude of ambiguity for the interferogram spanning August 1993 to August 1997 is $h_a > 10$ km. For an error in the DEM to create the two fringes observed in the interferogram, it would have to be $\epsilon = 2h_a = 20$ km in height and over 10 km in width.

Thus, we interpret these fringes as deformation on the ground. The circular fringes, centered on a point south of the Hrómundartindur volcanic system, correspond to uplift distributed over a roughly circular area with a radius of 10 km. In the 4-year interferogram, we count at least two fringes, corresponding to a relative shortening range of 6 cm in this area. We interpret this signature as mostly vertical uplift due to increasing pressure in a magma chamber below the Hromundartindur volcanic system.

3.1. Primary Signal: Magma Injection

To explain the concentric fringe pattern observed in the coherent interferograms, we assume that magma injection at depth causes the observed crustal deformation. Alternative explanations for the uplift exist (e.g., that it is caused by accumulation of water or gas), but we consider magma accumulation to be the most likely explanation. We approximate magma injection at depth as an increase in pressure within a small, sperical source buried in an elastic half-space [*Mogi,* 1958]. The elastic medium is a Poisson solid for which the two Lamé coefficients λ and μ are equal. Such a solid has a Poisson's ratio $\nu = 1/4$. Consquently, the ratio of P wave to S wave speeds is $V_p/V_s = \sqrt{3} = 1.73$. The approximation of a Poisson solid appears valid to within 4 % for the crust in the Hengill area (Plate 2a).

Equivalently, we have used *Okada's* [1985] formulation of a rectangular dislocation as a computational convenience for the Coulomb modeling described in section 4. We parameterize the source as tensile opening ($U_3 > 0$) on each of three mutually orthogonal 1-by-1-km dikes intersecting at their centers with the public domain RNGCHN program [*Feigl and Dupré,* 1999]. This approximation produces a displacement field at the Earth's surface which is indistinguishable from the conventional *Mogi* [1958] model, as we show in the electronic Appendix [1]. Both formulations have four parameters: latitude, longitude, depth d, and volume change ΔV of the source.

Using *Okada's* [1985] formulation for three orthogonal dikes, the volume change $\Delta V_{\mathrm{Okada}}$ is $3U_3LW$, where U_3 is the tensile opening, L the length, and W the width of each dike. In practice, we set $L = W = 1$ km and $\Delta V_{\mathrm{Okada}} = b\Delta V_{\mathrm{Mogi}}$, where b is a scaling factor needed to produce an equivalent displacement field at the surface. In our case, where the source is buried deep ($d \gg W$) within the Poisson solid, this scaling factor has a value of $b = 9/5$, as we derive in the elecronic Appendix. The half-space model provides a valid approximation because the source depth (7 km) is much larger than the topographic height of the edifice (0.4 km), lessening the need for more sophisticated models. Again we assume a Poisson solid since the expressions for surface displacement are independent of λ and μ in this case.

First, we locate the point source by trial and error comparison of observed and modeled interferograms. The horizontal position of the point source does not appear to vary significantly from one interferometric time interval to another (Figure 1b). Averaging over the 5-year interval from 1993 to 1998, we locate the point source at 64.032°N, 21.213°W ± 1 km. We assume this location to be constant. It is more precise than, farther south than, and consistent with the location derived from leveling between 1993 and 1995 [*Sigmundsson et al.,* 1997a].

Next, we vary the strength and depth of the source. For the interval from 1993 to 1998, we find an average depth of 7 ±2 km and average uplift rate above the source of $h_0/\Delta t = 19 \pm 2$ mm/yr (Figure 2a). Both these values are consistent with GPS and leveling measurements over the same period [*Sigmundsson et al.,* 1997a; *Hreinsdottir,* 1999].

To evaluate the uncertainty of these estimates, we set the 1σ confidence interval to the extreme values of the parameters corresponding to an ensemble of models with an equally

[1] A supporting derivation is available via Web browser or Anonymous FTP from ftp://kosmos.agu.org, directory "append" (Username = "anonymous", Password = "guest"); subdirectories in the ftp site are arranged by paper number. Information on searching and submitting electronic supplements is found at http://www.agu.org/pubs/esupp_about.html.

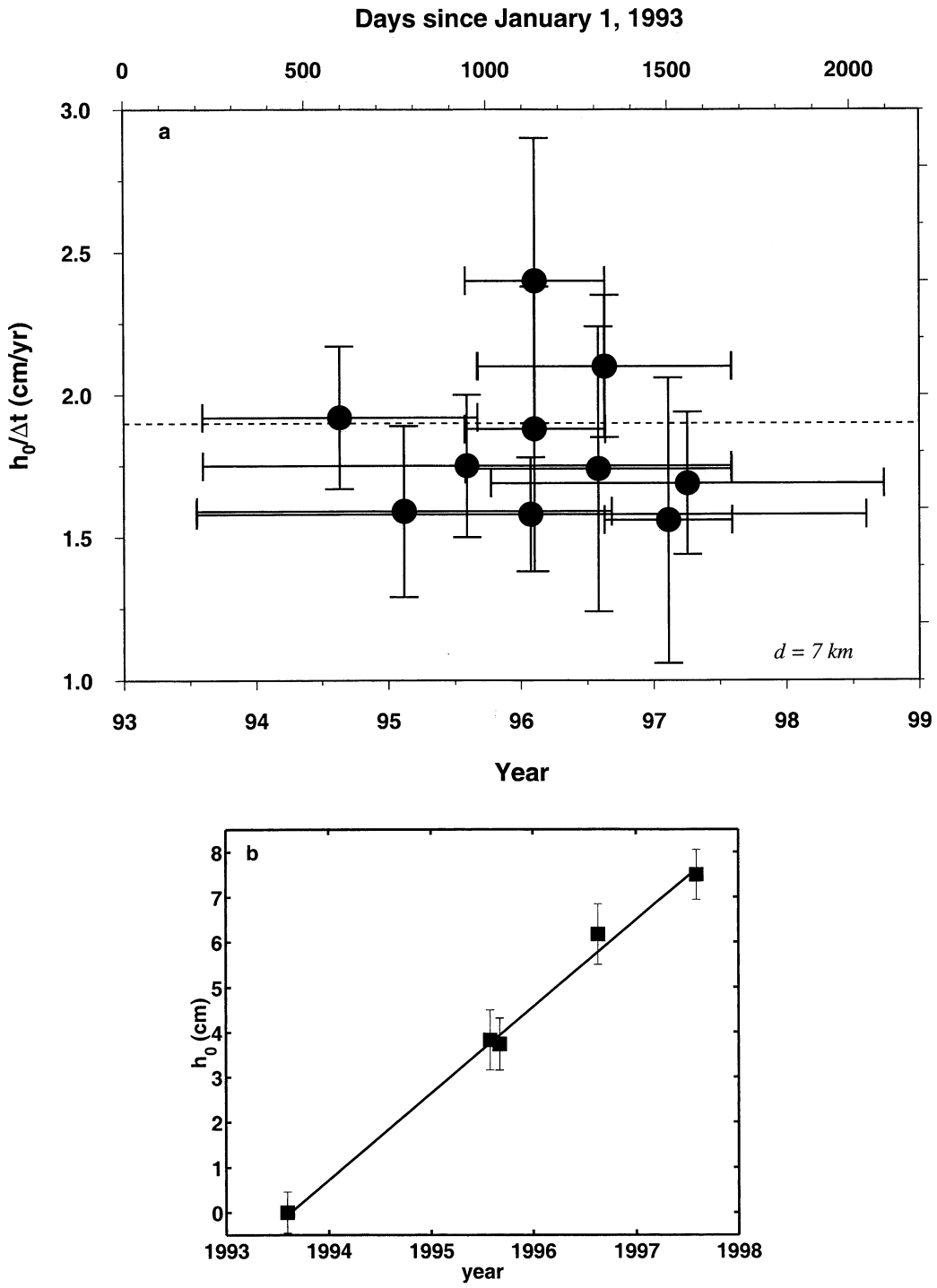

Figure 2. (a) Uplift rate in the Hengill area for the 1993-1998 interval determined by fitting the observed interferograms with an inflationary volume source at 7 km depth. Horizontal bars represent the interval of time spanned by the interferograms. Black circles show the maximum uplift h_0 over the pressure source divided by the time interval Δt of the interferogram. The uplift rate is fairly constant at 1.9 ± 0.2 cm/yr as denoted by the dashed line. (b) Uplift h_0 above the volume source as a function of time determined by estimating a pseudoabsolute parameter for each acquisition epoch.

good fit. In practice, such models fit the observed fringe pattern within about one quarter of a fringe, or 7 mm in range. This misfit is somewhat larger than the error expected from topographic errors in the DEM alone $\epsilon/h_a \approx 20$ m/200 m $\approx$ 1/10 fringe ≈ 3 mm, suggesting that the residual error is not topographic.

To clarify the temporal evolution of the strength of the magmatic source, we estimate its "pseudoabsolute" value

$[m_1, m_2, ...m_n]$ at individual points in time (the acquisition epochs) instead of its relative value $[m_{12}, m_{13}, ...m_{n-1,n}]$ over intervals of time (between the acquisition epochs). This we do by a simple inversion $\mathbf{Ax} = \mathbf{d}$, where the parameters $\mathbf{x}$ pertain to epochs, but the data $\mathbf{d}$ pertain to intervals. The elements in the design matrix $\mathbf{A}$ are either -1, 0, or 1. This procedure is analogous to adjusting a "free network" in classical geodesy in that the pseudoabsolute estimates are only determined relative to a single additive constant. It was first applied to interferograms by *Beauducel et al.* [2000]. The results appear in Figure 2b with error bars of ± 7 mm. The slope of this line is $h_0/\Delta t = 19 \pm 2$ mm/yr, confirming the constant uplift rate derived from the relative determination.

3.2. Faulting

Some of the interferograms show a linear discontinuity superimposed on the circular concentric pattern. Centered at 64.0281°N and 21.3051°W (±100 m), it is over 3 km in length and strikes N12 °E in azimuth (Plate 1c). We can interpret it using pair-wise logic, since the discontinuity appears on several interferograms covering different time intervals. We show two interferograms for the case where the discontinuity appears (Plates 2b & 2c and Figures 3a & 3b) and two more for the case where the discontinuity does not (Plates 2d & 2e and Figures 3c & 3d).

The discontinuity is present in all the interferograms spanning the interval between the acquisition dates of images 1452 and 21626, i.e. between July 31 and September 3, 1995, inclusive. Furthermore, the discontinuity does not appear in any of the interferograms before or after this time interval. This implies that the fringe pattern broke during this time interval.

Three phenomena could produce such a signature. The first possibility is an atmospheric effect. It cannot be an atmospheric artifact in the image acquired September 3, 1995 (image 21626), because the discontinuity appears in the interferograms including this image and spanning intervals before this date (Plate 2b), but does not appear in interferograms including this image and spanning intervals after this date (Plate 2e). The same type of argument excludes atmospheric artifacts for the other interferograms. Moreover, the crenulated shape of an atmospheric heterogeneity is unlikely to produce such a sharp discontinuity [e.g., *Massonnet and Feigl,* 1995, 1998].

The second possibility is a topographic error in the DEM. A steep cliff or scarp on the ground might be averaged across several DEM pixels, causing an unmodeled discontinuity in the interferometric fringe pattern. Or a scarp-like discontinuity might exist in the DEM but not on the ground. In either case, the error in the DEM would lead to the same discontinuity in the interferogram.

Three lines of reasoning argue against the hypothesis of a topographic error in the DEM. First, such an error should affect all interferograms calculated with the DEM. This is not the case, as observed by the clear fringe pattern in Plate 2d where the phase is continuous across the line in question. Second, the discontinuity also appears in interferograms calculated with an independent, but coarse, DEM. Third, the discontinuity appears in an interferogram with $|h_a| > 10$ km (Plate 1d) but also in interferograms with lower $|h_a|$ (e.g., Plate 2b). In both cases, the phase change is about one quarter of a cycle and so is not proportional to h_a.

Next, we consider the possibility of an artifact related to a topographic scarp. The southern two thirds of the discontinuity in the interferogram cut across a lava flow in the field. Although quite blocky and difficult to walk on, this flow is topographically fairly flat, with no feature exceeding 10 m from peak to trough, well below the senstivity of the worst-case interferogram in Plate 2c where $h_a = 226$ m. In this case, the offset across the discontinuity measures one quarter of a fringe, which would require a DEM error of $h_a/4 = 56$ m, about twice the precision of the DEM. At the field location corresponding to the northern third of the discontinuity, we found a steep slope with 50 m of total relief. Indeed, this segment is mapped as a normal fault scarp [*Saemundsson,* 1995]. It is a rocky cliff above an oversteepened scree slope. For such a scarp to cause the discontinuity in the interferogram, it would have to be incorrect or omitted in the DEM. Yet this steep slope appears correctly on both DEMs and on the (paper) map with a contour interval of 20 m and a scale of 1:25,000 [*Icelandic Geodetic Survey,* 1997]. Thus we deduce that the discontinuity cannot be the result of a topographic error in the DEM.

The discontinuity in the interferogram must therefore represent a discontinuity on the ground, which we interpret as a fault. We can measure its strike (N12°E) and length (3 km) directly from the interferogram (Plate 2b). The color changes from red to orange to yellow to green to blue on a path from west to east toward the center of the concentric fringes, indicating decreasing range change and increasing uplift. At the discontinuity, however, the color jumps directly from red to yellowish green, omitting orange and most of yellow. The sense of the phase jump is the same as that of the phase ramp: range decreases to the east. In other words, the block on the west side of the fault moved away from the satellite.

To measure the magnitude of the slip vector $\mathbf{U}$, we must assume its orientation. We consider three simple cases: pure strike slip ($\mathbf{U} = [U_1, 0, 0]$), pure dip slip ($\mathbf{U} = [0, U_2, 0]$), and pure tensile opening ($\mathbf{U} = [0, 0, U_3]$). In the strike-slip case, the motion is right lateral and the quarter-fringe offset in phase implies $U_1 = 27$ cm of slip. Although right-lateral strike slip on north striking faults is compatible with earthquake focal mechanisms in the current sequence [*Sigmundsson et al.,* 1997a], such a large throw is not observed in the field.

In the dip-slip case the motion implies normal faulting such that the west side (hanging wall block for the mapped westward dip) moves downward relative to the east side (footwall block). This is compatible with the interpolation of two fault segments on the geologic map [*Saemundsson,* 1995]. In this case the phase offset implies only $U_2 = 8$ mm of slip for a vertical fault. Although small, this amount of movement is supported by observations in the field. In July

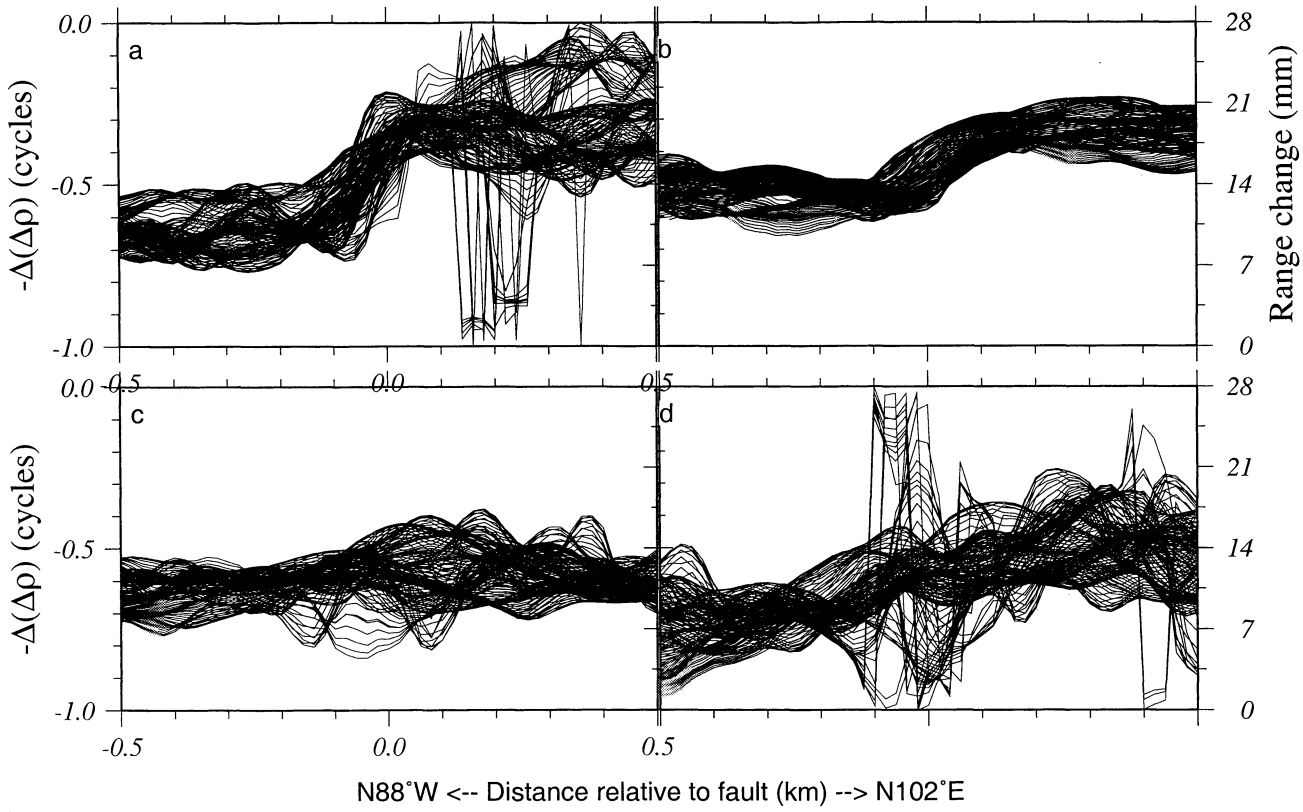

Figure 3. (a)-(d) Phase profiles corresponding to Plates 2b-2e. The profiles are perpendicular to the fault strike. The change in phase across profiles in Figures 3a and 3b, spanning August 1995, is about one quarter of fringe or 7 mm of range-shortening motion toward the satellite. We interpret this as 8 mm of normal-faulting motion with the west side dropping downward with respect to the east side.

1999 we found disturbed soil; fallen, broken, and cracked rocks; and killed moss and lichen both along the trace of the normal fault mapped in the overly steep slope and along its continuation in the Holocene lava field. Although circumstantial, all these observations appeared fresh enough be compatible with motion 4 years earlier in August 1995.

Alternatively, if the causal event were instead a dike, then we would infer U_3 =17 mm of tensile opening. Although such opening might explain our observations in the field, we would expect it to produce a fissure or tension gash. We observed no such features in the field. Furthermore, such a feature is not compatible with the mapped normal fault.

Yet this rupture did not register on seismometers because no earthquake larger than magnitude $M_l > 3.5$ occurred within 5 km during the interval identified in the interferograms. Yet 8 mm of normal slip on a fault 3 km long and 1 km wide corresponds to a magnitude M =3.9, again assuming a shear modulus of μ = 33 GPa. For the strike-slip case the corresponding magnitude would be M = 4.9. For the tensile opening dike it would be M = 4.2. If it broke brittle rock, such an event would register in the Icelandic Meteorological Office catalog, which is complete to magnitude 1 or 2, based on the corner in the Gutenburg-Richter frequency-magnitude distribution for this area and time. Although such an event might be associated with harmonic tremor at the time of dike injection, no tremor has been observed. The detection threshold for earthquakes in the Hengill area is close to M = 0 since 1997 [*Rognvaldsson et al.*, 1998a].

Thus we conclude that the break in fringe pattern corresponds to a break in the ground surface sometime in the interval July 31 through September 3, 1995. It is most likely to be 8 mm of downdip (west side down) slip on the mapped normal fault. The motion appears to be aseismic and may involve the only uppermost layer of broken rock.

Similar motion occured on the Almannagja fault, located in the Hengill fissure swarm north of Lake Thingvallavatn. Geodetic surveys between 1973 and 1977 suggest that the near-surface portion of the Almannagja normal fault slipped 9 cm, whereas the largest recorded earthquake in the area during this time interval was $M \approx 3.4$ [*Tryggvason,* 1990].

Our interpretation of such events is that they are slow readjustments in the semibrittle uppermost layer of broken rock and/or soil in response to local perturbations in the stress field of the order of 1 bar. These perturbations may in turn be caused by a distant earthquake or an underlying magmatic source. In the particular case of Hengill they relate to the uplift process.

3.3. Earthquake Sequence Beginning in June 1998

In June 1998, the rate of seismic moment release accelerated again (Figure 4). The effects of the early part of this se-

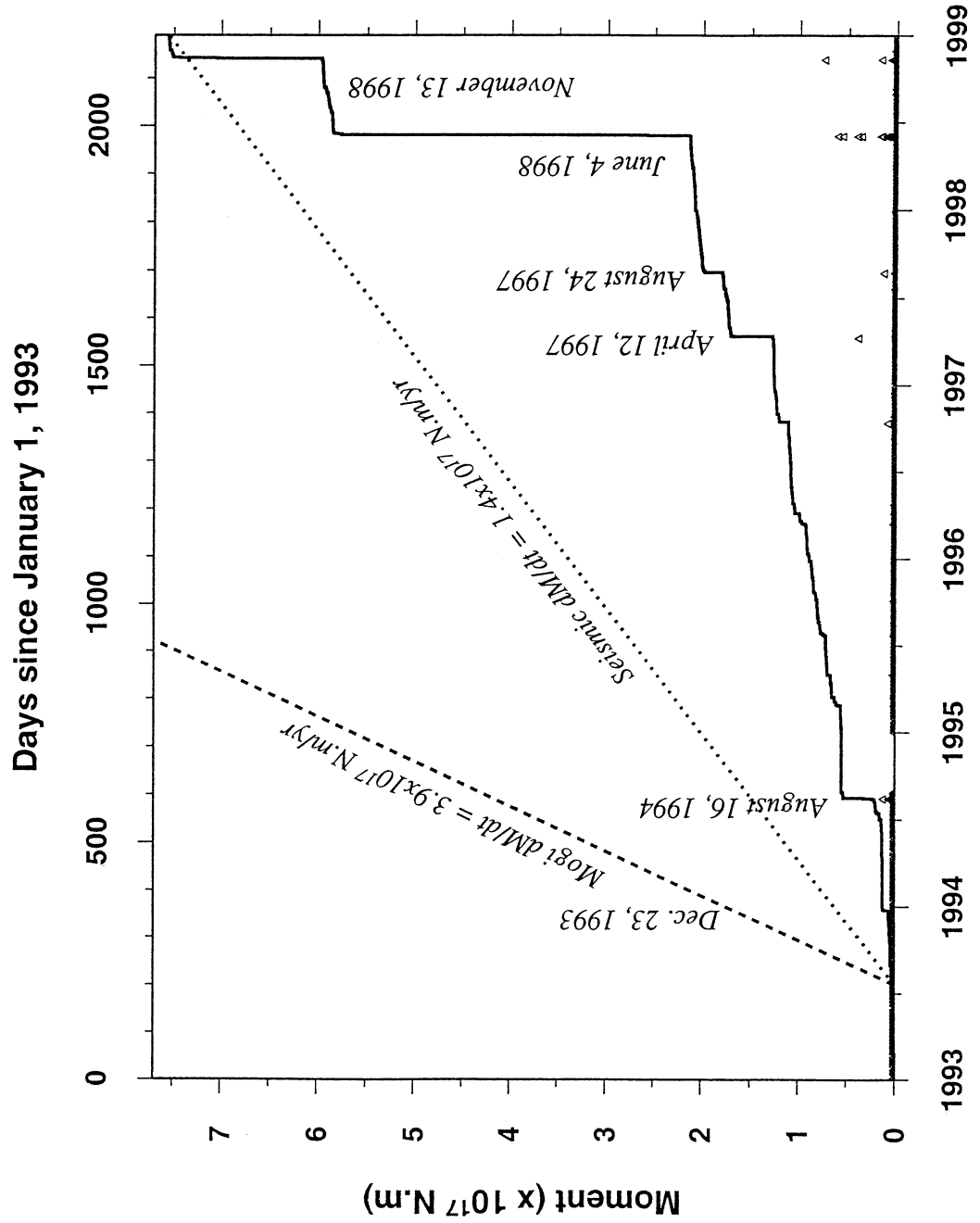

Figure 4. Moment as a function of time between 1992 and 1999, showing moment due to the Mogi volume source (dashed lines), cumulative seismic moment release from 1992 through 1998 (solid line), and daily seismic moment release rate (triangles) from the Icelandic Meteorological Office catalogue [*Rognvaldsson et al.*, 1998a, 1998b]. To provide an upper bound on the seismic moment rate, we have taken the larger of the two available estimates for which $\log(M)$ is either $1.5M_0 + 9.0$ or $1.3m_L + 10.5$ in N m [*Agustsson et al.*, 1999].

quence appear in the interferogram spanning 1995.8 1998.7 (Plate 1c).

This earthquake ruptured the soil-covered ground surface in a series of en-echelon cracks and fissures (A. E. Clifton, oral communication, 1999). The maximum opening of these fissures is 30 cm, with little or no strike- or dip-slip component. We cannot discern them in the interferogram.

Nonetheless, we wish to separate the coseismic deformation field associated with the June 4, 1998 earthquake from the magmatic inflation for the interferogram spanning 1995.8–1998.7 (Plate 1c). Toward that end, we consider a first-order model with a single nearly vertical fault striking N15°E, as suggested by the focal mechanism estimated from P wave first-arrival polarities and cosesismic displacement vectors measured by GPS (Thora Arnadottir, written communication, 1999). It involves 28 cm of right-lateral strike slip and 15 cm of dip slip. The modeled fault is 11 km long and extends from the surface to 2 km depth. Although the interferometric range change calculated from this model is 11 cm, the fringe pattern is very localized. It is also smaller and less symmetric than the concentric uplift fringes. The coseismic signature can thus be safely neglected in estimating the parameters for the magma injection model, especially since it affects only two interferograms. We do not consider this earthquake further in this paper.

4. Triggering of Earthquakes by Magma Injection

The magmatic inflation responsible for the concentric pattern we observe in the inter ferograms can perturb the stress field enough to trigger earthquakes. This has been suggested previously, for example, on the Izu Peninsula [*Thatcher and Savage,* 1982]. Using a Mohr-Coulomb criterion, these authors find that the stress changes of a few bars induced by inflation are in the correct sense to trigger the failure that occurred in large earthquakes in 1930 and 1978, but not 1980. In Iceland, magmatic activity appears to have triggered the 1987 Vatnafjoll earthquake [*Agustsson et al.,* 1999]. In Long Valley, California "the observation of significant volumetric expansion components in the moment tensors of the 1997 ... seismicity indicates a direct relation between at least some of the seismicity and hydrothermal or magmatic processes" [*Dreger et al.,* 2000, p. 125]. That volcanic eruptions can trigger earthquakes highlights the sensitive mechanical coupling between the two processes, as suggested by the significant temporal correlation between eruptions of Vesuvius and earthquakes in the Apennines [*Nostro et al.,* 1998]. Indeed, temporal sequences in the opposite sense, suggesting earthquakes triggering eruptions, have been documented at both the local and global scales [*Malone et al.,* 1981; *Bautista et al.,* 1996; *Linde and Sacks,* 1998].

Here we hypothesize that the inflation at 7 km depth triggers earthquakes in the brittle crust just above, as suggested previously on the basis of GPS and leveling surveys [*Sigmundsson et al.,* 1997a]. To test this hypothesis, we calculate the change in Coulomb failure stress induced by the same small volumetric source model used to fit surface deformation field recorded by the interferograms. We perform this calculation using version 1 of the Almond software written by G. C. P. King. This program employs the three-dimensional formulation derived by *Okada* [1992]. We have multiplied the resolved stresses by a factor of 2 to account for the notational glitch described by *Hubert-Ferrari et al.* [2000].

We model the source as three mutually orthogonal dikes intersecting at a point 7 km below the center of the concentric fringes. Each dike is 1 km square and opens as a tensile crack with U_3 set to 12 m, corresponding to 5 years' accumulation of the average volume change rate, as estimated from the interferograms.

We assume the apparent coefficient of friction μ'_f to be 0.4. This value has become conventional for this type of triggering study because it minimizes the calculation error to ± 25 % [*King et al.,* 1994; *Stein,* 1999]. It is equivalent to a coefficient of static friction of 0.75, like the values of 0.6 to 0.8 used by *Thatcher and Savage* [1982] on the basis of laboratory experiments on crustal rocks [*Byerlee,* 1978].

We then calculate the Coulomb stress change that would be resolved on a fault if it were optimally oriented. The optimal strike is the one that maximizes the Coulomb stress. It depends on the friction coefficient and the regional stress field. The magma injection increases the Coulomb failure stress in a circular area. The diameter of this circle increases with the volume of the volcanic source and decreases with its depth. The stress increase is several times greater at 4 km depth, where most of the earthquakes occur.

To reproduce the narrow NE-SW pattern in the seismicity map, we include the effect of a regional stress field in which the axis of maximum compressive stress (σ_1) is horizontal and directed roughly NE-SW and the axis of minimum compressive stress (σ_3) is also horizontal and directed NW-SE. Their magnitudes are both set arbitrarily to 1 bar. The third component of the imposed regional stress field has zero magnitude along a vertical axis. Our modeling results are not very sensitive to the orientation or magnitude of the regional stress field.

Summing the Coulomb failure stress perturbations caused by the volume source and the regional stress field creates a circular pattern superimposed on four quadrants. The four quadrants resemble the shear strain field calculated previously [*Sigmundsson et al.,* 1997a]. Their orientation depends on the azimuth assumed for the regional stress field. The result is four lobes whose size depends on the relative magnitudes of the two input stress fields. The NE and SW lobes exhibit a positive Coulomb stress change (increase) exceeding 2 bar (0.2 MPa), favoring earthquakes there. These include right-lateral strike slip on N-S striking vertical faults, as indicated by focal mechanisms in the Hengill area [*Sigmundsson et al.,* 1997a] and the adjacent Southern Iceland Seismic Zone [*Sigmundsson et al.,* 1995] as well as structural trends [*Einarsson,* 1991; *Luxey et al.,* 1997; *Bergerat et al.,* 1998].

Plate 3a shows the Coulomb stress change on a horizontal

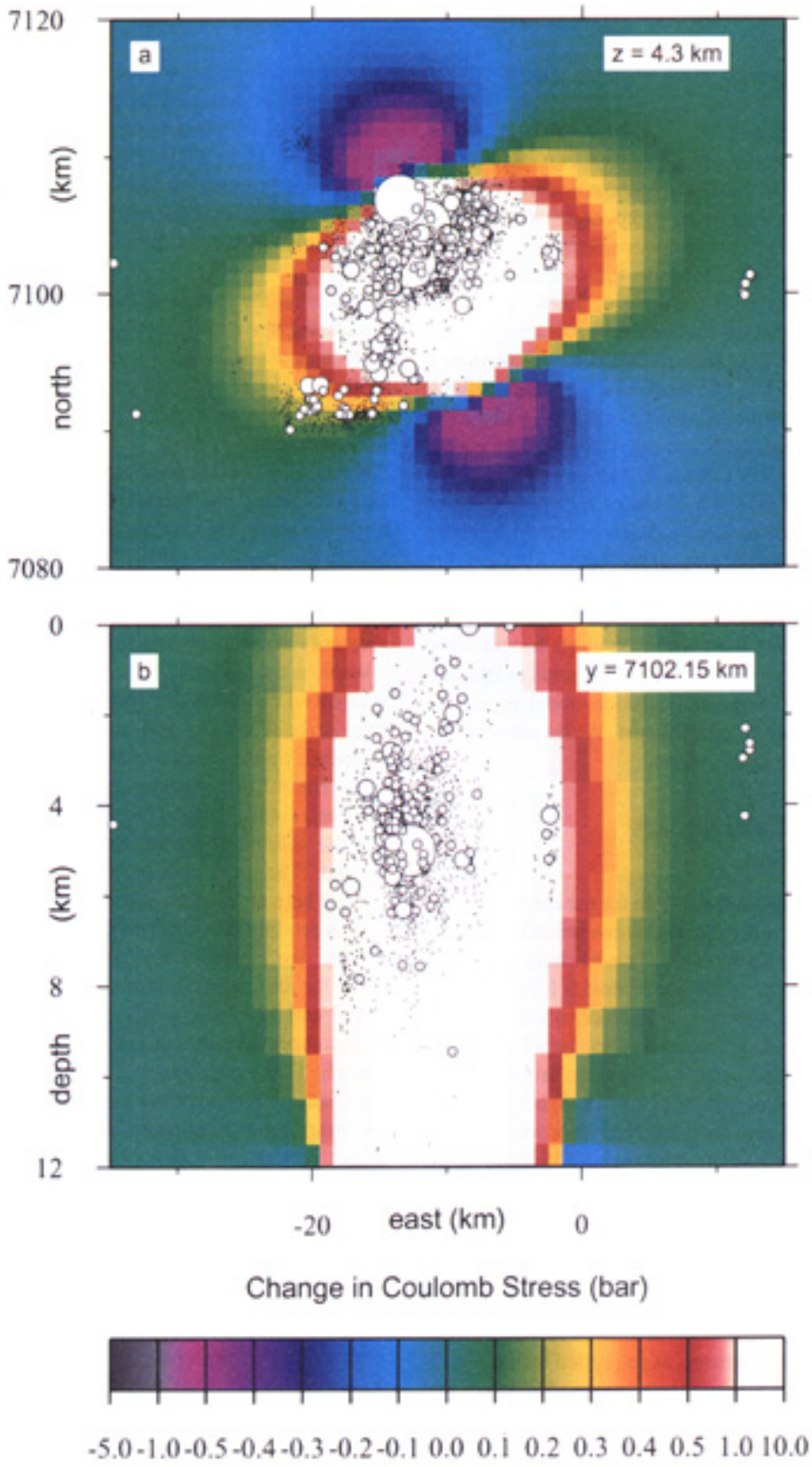

Plate 3. (a) Coulomb failure stress change on optimally oriented vertical faults shown in a horizontal slice at 4.3 km depth. White color denotes where the stress increase is >1 bar but <10 bar. Source parameters include: latitude 64.032°N, longitude 21.213°W, depth 7.0 km, tensile opening $U_3$12.1 m on each of three dikes with length $L = 1$ km and width $W = 1$ km; the apparent coefficient of friction $\mu'_f = 0.4$, the azimuth $\phi = 70°$ (measured clockwise from north) of the most compressive principal value of the stress tensor, and its magnitude $|\sigma_1| = 1$ bar, and the two Lame' constants $\mu = \lambda = 33$ GPa. Earthquakes hypocenters (circles and dots) are as in Plates 1 and 2. (b) Coulomb failure stress change on optimally oriented vertical faults shown in a vertical cross section passing East-West through the center of the modeled volcanic point source (crossed square). Model parameters and plotting conventions as in Plate 3a.

slice at 4.3 km depth, the average value for earthquakes in the 1994–1998 swarm. Plate 3b shows a vertical cross section. Most (84%) of the earthquakes recorded between 1993 and 1998 occur in areas where the Coulomb stress increases by > 0.6 bar, indicating that they were indeed triggered by the magmatic injection. Conversely, however, the Coulomb stress increase is large in many areas where no earthquakes occur. In other words, the locus of earthquake hypocenters is offset to the northwest of the volume source (square in Plates 3a). We will consider several explanations for this observation below.

We use the "triggering percentage" as a statistic to evaluate the soundness of our assumptions. It is a reasonable way to score various models despite the fact that it does not account for the fact that smaller earthquakes are more likely than large ones to be mislocated in the seismological catalog. Yet a scoring scheme weighted by earthquake magnitude would favor large events, which are no more likely to be triggered by the magmatic source than small events. This is because the Coulomb failure mechanism does not necessarily imply a correlation between triggering stress and earthquake magnitude.

A slightly smarter scoring scheme would give a higher score to events triggered in areas of high Coulomb stress increase than to areas of stress decrease. For this score, we multiply the number of earthquakes with magnitude larger than 1 in a cell by the Coulomb stress change there. This yields a value in units of pressure which we call the "trigger score" S.

We consider several sets of assumptions, as listed in Table 2. Our preferred model is the one described above and shown in Plate 3.

Table 2. Results of Various Tests on Triggering Model Parameters

μ'_f	ϕ	$\lvert\sigma_1\rvert$, bar	Percent	S, bar
0.4	70°	1	83.	6974.
0.4	70°	0.1	87.	7062.
0.4	70°	10	64.	5122.
0.4	70°	30	47.	2404.
0.4	20°	1	84.	6978.
0.4	30°	1	84.	6980.
0.4	60°	1	83.	6998.
0.4	70°	1	83.	6974.
0.4	80°	1	83.	6976.
0.0	30°	1	87.	7146.
0.4	30°	1	84.	6980.
0.6	30°	1	84.	7254.
0.8	30°	1	84.	7718.
1.0	30°	1	84.	8306.

We varied the values for: the apparent coefficient of friction μ'_f, the azimuth ϕ (measured clockwise from north) of the most compressive principal value σ_1 of the stress tensor, and its magnitude $|\sigma_1|$. The percent gives the triggering percentage of earthquakes which occur in areas of Coulomb stress increase > 0.6 bar. The alternative scoring statistic S of the number of earthquakes in a map cell times the Coulomb failure stress change there in bars. The first row describes the preferred model shown in Plate 3.

5. Discussion

Before interpreting our results in terms of volcanic processes, we review the energy fluxes in the Hengill volcanic system. The magma source is inflating at a fairly constant rate of $3.9 \pm 0.4 \times 10^6 \mathrm{m}^3/\mathrm{yr}$, using the Mogi approximation in a Poisson solid. This accumulates as elastic deformation energy in the host rock. The scalar moment for such a source is $M_0 = 3\mu\Delta V = 4\pi\mu h_0 d^2$ (M. Bonafede, written communication, 1999, correcting a topographic error in *Langbein et al.* [1993]). We also assume the conventional value $\mu = 33$ GPa, as we will discuss below. Under these assumptions we find the rate of moment accumulation to be $3.9 \pm 0.4 \times 10^{17}$ N m/yr over the 1993-1998 interval (Figure 4). This value is 2.8 times faster than the rate of seismic moment release, 1.4×10^{17} N m/yr. For comparson, this rate ratio is over 40 at Long Valley Caldera [*Langbein et al.,* 1993].

If we expect the seismic and volcanic processes to balance, we should consider different values for the shear modulus. The basaltic rock in the geothermally active Hengill area must contain fissures, fluids, and altered minerals. All three of these will lower both the density ρ and the P wave velocity V_P from the typical values of 2.6 to 3.3 $\mathrm{g/cm}^3$ and 4.5 to 6.0 km/s, respectively, measured in the basaltic sections of the Oman ophiolite [*Christensen and Smewing,* 1981]. By assuming severe alteration, we might find a density as low as $\rho = 2.4$ $\mathrm{g/cm}^3$ and a P wave velocity as low as $V_P = 4.0$ km/s. These values are compatible with the seismic tomography study at Hengill [*Miller et al.*, 1998]. In this case, we find a shear modulus of $\mu = \rho V_P^2/3 = 13$ GPa. To make the two rates balance would require a shear modulus of $\mu = 12$ GPa. Such low values are compatible with P-wave velocity V_P values as low as 3.2 to 3.5 km/s measured at room temperature in fresh Icelandic basalt after thermal fracturing at 800°C (P. Meredith, written communication, 2000).

If the shear modulus is higher than 12 GPa, then there is an imbalance in power. We consider three possible explanations in order of decreasing likelihood. If the crust is not elastic, then the inflationary deformation does not accumulate as elastic strain energy. Instead, it dissipates inelastically as heat. For example, if the injected magma induced viscous or plastic flow in the lower crust, then the value of M_0 we calculate from the Mogi model would overestimate the moment. That the rheology is more complex than a simple elastic solid is also suggested by the deviations in V_P/V_S from the value of 1.73 expected for a Poisson solid (Plate 2a).

Second, the deformation may be accumulating as elastic strain energy to be released in a future earthquake. The rate of moment released by earthquakes during the active interval 1997–1998 is 3×10^{17} N m/yr (Figure 4). In this case, the seismic deficit accumulated between 1993 and the end of 1998 is roughly 13×10^{18} N m, equivalent to a magnitude 6 earthquake. Since our model calculates static stresses, it cannot say anything about the timing of such an event.

Third, the accumulating elastic strain energy may be released in a future volcanic event. In light of the small deficit

of $\sim 10^{18}$ J, such an event is likely either to be fairly small or to occur in the distant future.

Unfortunately, neither our data nor our models can distinguish between these three cases.

Although the orientation of the maximum compressive principal stress σ_H is essentially NE-SW, the estimates vary somewhat. Focal mechanisms around Hengill indicate an average azimuth of N53°E for σ_H [*Rognvaldsson et al.,* 1998a]. Yet borehole studies near the eastern end of the SISZ, over 50 km from Hengill, suggest azimuths ranging from N21°E to N80°E [*Stefansson et al.,* 1999]. Here we have attempted to estimate the orientation of σ_H by trial-and-error use of the stress triggering model, assuming that the best fitting model is the one which best predicts the locations of earthquakes. Yet neither of the two statistics for quantifying such a fit, triggering percentage or the stress-weighted score S, is particularly sensitive to the orientation or magnitude of the regional stress field. Almost any reasonable regional stress field with horizontal compression σ_H oriented NE-SW will produce a four-lobed pattern which breaks the circular symmetry of the volcanic source.

The magnitude of the assumed regional stress field is even less well determined by our modeling. Values from 0.1 to 10 bar all provide acceptable fits, as shown in Table 2.

All of the models in this class predict high, positive values of Coulomb failure stress change in the quadrants to the northeast and southwest of the magma source. Yet most of the earthquakes occur in the northwest quadrant, under the Hengill volcanic system, and almost none occur in the southeast quadrant, under the Grensdalur volcanic system. Why?

One (partial) explanation is that the earthquakes occur preferentially in cold, brittle rock. Indeed, seismic tomography reveals such a structure centered on, but a few kilometers above, our estimated position of the volcanic source [*Miller et al.,* 1998]. They find a large (10-km-wide), positive anomaly in P-wave velocity, which they interpret as solidified intrusions between about 1 and 5 km depth (dashed white contours in Plate 2a). Many earthquake hypocenters lie within this volume, presumably because it is cold and brittle. This structure is fairly symmetric about the volcanic source (like the area of increased Coulomb stress), with a maximum P wave velocity anomaly of $\delta V_P > +0.4$ km/s in the northeast quadrant at 3 to 4 km depth. Yet the round positive V_P anomaly is almost 4 times larger than the earthquake cluster. In other words, the cold brittle material, even when loaded, does not nucleate many earthquakes. It must also contain faults or through going fissures susceptible to rupture. If properly oriented, such structures could rupture by brittle failure in earthquakes with double-couple mechanisms, as predicted by our triggering model.

The other structural correlation is that the earthquakes seem to cluster in a volume where *Miller et al.* [1998] find a branch-shaped negative (-4%) anomaly in the ratio of P wave to S wave speeds ($V_p/V_s < 1.73$). Located in the geothermal area in the uppermost 4 km of the crust in the quadrant northeast of the volume source, this anomaly appears red in Plate 2a. According to *Miller et al.,* [1998, p. 309] the V_p/V_s anomaly "correlates with the geothermal field, but is too strong to be caused solely by the effect of temperature upon liquid water or the presence of vapor, and requires in addition mineralogical or lithological differences between the geothermal reservoir and its surroundings". These pipe-like structures look like the plumbing of the geothermal area. One such pipe sits directly above the position of the volcanic source estimated from the interferograms. Another intersects the cluster of earthquake hypocenters (Plate 2a). Indeed, many of the earthquakes, including two of the three largest events, cluster near the minimum $V_p/V_s < 1.73$ anomaly. We believe that the geothermal pipes include fissures and faults that provide the zones of weakness necessary for earthquake rupture.

The caveat to this explanation is that fissures and dikes in the geothermal area might be expected to change the rock volume. These would be non-double couple earthquakes with a significant component of tensile opening, which "may be fluid flow into newly formed cracks" [*Miller et al.,* 1998, p. 309]. The tensile component of such earthquakes is not accounted for by the shear Coulomb failure theory implicit in the stress-triggering model. Some 75% of the 70 well-constrained events that were captured in 1991 around the Hengill area had "significantly non-double couple mechanisms" [*Miller et al.,* 1998, p. 309]. On the other hand, the majority of the earthquakes recorded for the swarm beginning in 1994 are consistent with the doublecouple model, although some nondoublecouple events cannot be excluded [*Rognvaldsson et al.,* 1998a, 1998b].

Our model suggests that magmatic inflation can trigger earthquakes, with stress rising slowly to failure and then dropping instantaneously in an earthquake. Thus a plot of stress as a function of time on a given fault forms a sawtooth pattern. Prior to an earthquake, on the leading edge of the sawtooth, the stress increases at a rate of the order of $\sim$ 1bar/yr. After accumulating for a time interval Δt years, the stress then decreases abruptly in an earthquake with stress drop $\delta\tau$. For the magnitude 5.2 earthquake of June 4, 1998, we take a mean stress drop of the order of $\tau \sim 20$ bars, assuming that μ =33 GPa and $\delta\tau = \mu U(LW)^{1/2}$. If this rupture returns the state of its stress to its initial level, then the accumulation interval is of the order of $\Delta t \sim 20$ years. If this process is cyclical, then this interval is the recurrence time of a characteristic earthquake. It suggests that inflation of a magma chamber can furnish the primary driving force to actually break rocks on a fault in an earthquake.

6. Conclusions

INSAR can span 4 years in Iceland on bare volcanic rocks using images acquired during the snow-free summer months. The interferograms apparently record aseismic motion on a short segment of normal fault in August 1995, which slipped by 8 mm, corresponding to a geodetic moment magnitude of 3.9. Otherwise, the dominant signature is secular uplift, which we interpret as the result of increasing pressure caused by magma accumulation. An inflating volume source at 7 km depth in an elastic half-space describes the concentric deformation pattern well. The INSAR results determine the

source position to within ±1 km and the uplift rate to be 19 ± 2 mm/yr. Both parameters are constant from 1993 to 1998, although the seismic activity is episodic. Calculations of Coulomb failure stress suggest that injection of magma into the shallow crust may trigger fault slip.

Acknowledgments. We dedicate this paper to the memory of Sigurdur Rognvaldsson, who inspired all who knew his work. We thank Wayne Thatcher, Pall Einarsson, Ragnar Stefansson, and Thora Arnadottir for interesting discussions. We gratefully acknowledge the contributions of Geoff King, who graciously provided his Almond software; Maurizio Bonafede, who generously helped us with the math; Zhong Lu, who carefully wrote ps_filt2; and Gillian Foulger, who patiently shared tomographic grid files. Susan Owen, Kristjan Agustsson, and Alan Linde all provided constructive reviews. All figures were made using the public domain GMT software [*Wessel and Smith,* 1998]. J.G. acknowledges a doctoral fellowship from the French MENERT. The European Space Agency holds the copyright to all the ERS-1 and ERS-2 data used in this study, some of which were provided under the terms of ERS AO3-200. The DIAPASON software developed by the CNES was licensed to GDR INSAR. This work was supported under European Community contracts ENV4-CT96-0252 and ENV4-CT97-0536+A6 to the PRENLAB and PRENLAB-2 projects.

References

Agustsson, K., A.T. Linde, R. Stefansson, and S. Sacks, Strain changes for the 1987 Vatnafjöll earthquake in south Iceland and possible magmatic triggering, *J. Geophys. Res., 104,* 1151-1162, 1999.

Bautista, B. C., M. L. P. Bautista, R. S. Stein, E. S. Barcelona, R. S. Punongbayan, E. P. Laguerta, A. R. Rasdas, G. Ambubuyog, and E. Q. Amin, Relationship of Regional and Local structures to Mount Pinatubo activity, in *Fire and Mud: The 1991 Eruption of Mount Pinatubo, Philippines*, edited by C.G. Newhall, pp. 351-370, Univ. Wash. Press, Seattle, 1996.

Beauducel, F., P. Briole, and J. L. Froger, Volcano wide fringes in ERS synthetic aperture radar interferograms of Etna: Deformation or tropospheric effect?, *J. Geophys. Res., 105,* 16,391-16,402, 2000.

Bergerat, F., A. Gudmundsson, J. Angelier, and S. T. Rögnvaldsson, Seismotectonics of the central part of the South Iceland Seismic Zone, *Tectonophysics, 298,* 319-335, 1998.

Byerlee, J., Friction of rocks, *Pure Appl. Geophys., 116,* 615-626, 1978.

Centre National d'Etudes Spatiales (CNES), DIAPASON software package, Toulouse, France, 1997.

Christensen, N. I., and J. D. Smewing, Geology and seismic structure of the northern section of the Oman ophiolite, *J. Geophys. Res., 86,* 2545-2555, 1981.

Dreger, D.S., H. Tkalcic, and M. Johnston, Dilational processes accompanying earthquakes in the long valley caldera, *Science, 288,* 122-125, 2000.

Einarsson, P., Earthquakes and present-day tectonism in Iceland, *Tectonophysics, 189,* 261-279, 1991.

Feigl, K.L., and E. Dupré, RNGCHN: A program to calculate displacement components from dislocations in an elastic half-space with applications for modeling geodetic measurements of crustal deformation, *Comput. Geosci., 25,* 695-704, 1999.

Gasperi, J., Etude de la dformation lithosphrique active par interfromtrie radar. Application la region de Hengill, Islande, Ph.D. thesis, Univ. P. Sabatier, Toulouse, France, 1999.

Goldstein, R.M., and C.L. Werner, Radar interferogram filtering for geophysical applications, *Geophys. Res. Lett., 25* (21), 4035-4038, 1998.

Hreinsdottir, S., GPS geodetic measurements on the Reykjanes Peninsula, SW Iceland: crustal deformation from 1993 to 1998, M.S. thesis, Univ. of Iceland, Reykjavik, 1999.

Hubert-Ferrari, A., A. Barka, E. Jacques, S. S. Nalbant, B. Meyer, R. Armijo, P. Tapponnier, and G. C. P. King, Seismic hazard in the Marmara Sea region following the 17 August 1999 Izmit earthquake, *Nature, 404,* 269-273, 2000.

Icelandic Geodetic Survey, Hengill quadrangle topographic map, 1:25,000 scale, Reykjavik, 1997.

King, G. C. P., R. S. Stein, and J. Lin, Static stress changes and the triggering of earthquakes, *Bull. Seism. Soc. Amer., 84,* 935-953, 1994.

Langbein, J., D. P. Hill, T. N. Parker, and S. K. Wilkinson, An episode of reinflation of the Long Valley Caldera, eastern California, *J. Geophys. Res., 98,* 15,851-15,870, 1993.

Linde, A. T., and I. S. Sacks, Triggering of volcanic eruptions, *Nature, 395,* 888-890, 1998.

Luxey, P., P. Blondel, and L. M. Parson, Tectonic significance of the South Iceland Seismic Transform Zone, *J. Geophys. Res., 102,* 17,967-17,980, 1997.

Malone, S. D., E. T. Endo, C. S. Weaver, and J. W. Ramey, Seismic monitoring for eruption prediction, in *The 1980 Eruptions of Mount St. Helens, Washington*, edited by P. W. Lipman and D. R. Mullineaux, *U.S. Geol. Surv. Prof. Pap. 1250,* 803-813, Washington, DC, 1981.

Massonnet, D., and K. L. Feigl, Discrimination of geophysical phenomena in satellite radar interferograms, *Geophys. Res. Lett., 22,* 1537-1540, 1995.

Massonnet, D., and K.L. Feigl, Radar interferometry and its application to changes in the Earth's surface, *Rev. Geophys., 36,* 441-500, 1998.

Massonnet, D., and F. Sigmundsson, Remote sensing of volcano deformation by radar interferometry from various satellites, in *Remote sensing of active volcanism, Geophys. Mongogr. Ser.*, vol. 116, edited by P. Mouginis-Mark, J. A. Crisp, and J. H. Fink, 207-221, AGU,Washington, D. C., 2000.

Miller, A. D., B. R. Julian, and G. R. Foulger, Threedimensional seismic structure and moment tensors of nondouble couple earthquakes at HengillGrensdalur volcanic complex, Iceland, *Geophys. J. Int., 133,* 309-325, 1998.

Mogi, K., Relations between the eruption of various volcanoes and the deformations of the ground surfaces around them, *Bull. Earthquake Res. Inst. Univ. Tokyo, 36,* 99-134, 1958.

Nostro, C., R. S. Stein, M. Cocco, M. E. Belardinelli, and W. Marzocchi, Two-way coupling between Vesuvius eruptions in southern Apennine earthquakes, Italy, by elastic stress transfer, *J. Geophys. Res., 103,* 24,487-24,504, 1998.

Okada, Y., Surface deformation to shear and tensile faults in a half-space, *Bull. Seism. Soc. Am., 75,* 1135-1154, 1985.

Okada, Y., Internal deformation due to shear and tensile faults in a half space, *Bull. Seism. Soc. Am., 82,* 1018-1040, 1992.

Rognvaldsson, S. T., G. B. Gudmundsson, K. Agustsson, S. S. Jakobsdottir, R. Slunga, and R. Stefansson, Overview of the 1993-1996 seismicity near Hengill, *report VI R98006-JAO5*, Icelandic Meterological Office, Reykjavik, 1998a.

Rognvaldsson, S. T., et al., Earthquake swarm in Olfus in Novemeber 1998, in Icelandic with an English summary, *report VI-G980446-JA09*, Icel. Meterol. Off., Reykjavik, 1998b.

Saemundsson, K., Hengill, geological map (bedrock) scale 1:50.000, Orkustofnun, Hitaveita Reykjavíkur and Landmaelingar Íslands, Reykjavik, 1995.

Sigmundsson, F., P. Einarsson, R. Bilham, and E. Sturkell, Rift-transform kinematics in south Iceland: Deformation from Global Positioning System measurements, 1986 to 1992, *J. Geophys. Res., 100,* 6235-6248, 1995.

Sigmundsson, F., P. Einarsson, S. T. Rognvaldsson, G. R. Foulger, K. M. Hodgkinson, and G. Thorbergsson, The 1994-1995 seismicity and Deformation at the Hengill triple junction, Iceland: Triggering of earthquakes by minor magma injection in a zone

of horizontal shear stress, *J. Geophys. Res., 102,* 15,151-15,161, 1997a.

Sigmundsson, F., H. Vadon, and D. Massonnet, Readjustment of the Krafla spreading segment to crustal rifting measured by Satellite Radar Interferometry, *Geophys. Res. Lett., 24,* 1843-1846, 1997b.

Stefansson, R., F. Bergerat, M. Bonafede, R. Bodvarsson, S. Crampin, K. L. Feigl, F. Roth, F. Sigmundsson, and R. Slunga, PRENLABTWO first annual report, *Rep. VI-G99016-JA05*, Icel. Meterol. Off. Reykjavik, 1999.

Stein, R. S., The role of stress transfer in earthquake occurrence, *Nature*, *402*, 605-609, 1999.

Thatcher, W., and J. C. Savage, Triggering of large earthquakes by magma-chamber inflation, Izu Peninsula, Japan, *Geology*, *10*, 637-640, 1982.

Tryggvason, E., Displacement of the Almannagja fault: Measurements at Thingvellir 1990, *Rep. 9001*, Nord. Volcanol. Inst., Reykjavik, 1990.

Vadon H., and F. Sigmundsson, Crustal deformation from 1992 to 1995 at the Mid-Atlantic ridge, southwest Iceland, mapped by satellite radar interferometry, *Science, 275,* 193-197, 1997.

Wessel, P., and W. H. F. Smith, New, improved version of generic mapping tools released, *Eos Trans. AGU*, *79*, 579, 1998.

K. L. Feigl, J. Gasperi, and A. Rigo, UMR 5562, 14 ave. Edouard Belin, 31400 Toulouse, France. (Kurt.Feigl@cnes.fr; gasperi@pontos.cst.cnes.fr; Alexis.Rigo@cnes.fr)

F. Sigmundsson, Nordic Volcanological Institute, University of Iceland, Grensavegur 50, IS-108 Reykjavik, Iceland. (fs@norvol.hi.is)

(Received October 13, 1999; revised May 4, 2000;
accepted June 9, 2000.)